

The Geodesic Distance between \mathcal{G}_I^0 Models and its Application to Region Discrimination

José Naranjo-Torres, Juliana Gambini, and Alejandro C. Frery

Abstract—The \mathcal{G}_I^0 distribution is able to characterize different regions in monopolarized SAR imagery. It is indexed by three parameters: the number of looks (which can be estimated in the whole image), a scale parameter, and a texture parameter. This paper presents a new proposal for feature extraction and region discrimination in SAR imagery, using the geodesic distance as a measure of dissimilarity between \mathcal{G}_I^0 models. We derive geodesic distances between models that describe several practical situations, assuming the number of looks known, for same and different texture and for same and different scale. We then apply this new tool to the problems of identifying edges between regions with different texture, and quantify the dissimilarity between pairs of samples in actual SAR data. We analyze the advantages of using the geodesic distance when compared to stochastic distances.

Index Terms—Geodesic distance, SAR image interpretation, texture measure.

I. INTRODUCTION

AUTOMATIC interpretation of SAR (*Synthetic Aperture Radar*) images is challenging. It has important applications in, for instance, urban planning [1]–[3], disaster management [4]–[7], emergency response [8], [9], environmental monitoring and ecology [10]–[13]. One of the most important topics is the automatic discrimination of regions with different levels of texture or roughness.

Surface roughness is, along with the dielectric properties of the target, an important parameter. It can be related to parameters of the imaging process as, for instance, resolution [14], but it can also be described by statistical models.

Several statistical models have been presented for image classification [15], target detection and recognition [16] and segmentation [17]–[20]. In recent years, speckled data have been modeled under the multiplicative model using the \mathcal{G} family of

distributions [21]. This model is able to describe extremely textured areas better than the \mathcal{K} distribution [22], [23]. Gao [24] discusses several statistical models and their relationships.

The \mathcal{G}_I^0 distribution is able to characterize regions with different degrees of texture in monopolarized SAR imagery [21]. It depends on three parameters: the equivalent number of looks L , which is considered known or can be estimated for the whole image, the texture parameter α , and the scale parameter γ ; the last two may vary locally. One of the most important features of the \mathcal{G}_I^0 distribution is that α can be interpreted in terms of the roughness or texture of the observed area, which is related to the number of elementary backscatters per cell, so it is important to infer about it with quality [25]. In this paper, we use maximum likelihood estimation because its asymptotic properties are known to be excellent.

The problem of comparing two or more samples using distances or divergences, prevails in image processing and analysis. Several authors employ information-theoretic measures of contrast among samples in classification [26], [27], edge detection [28]–[33], saliency detection [34], and despeckling [35]. In the article [36], the authors use the concept of mutual information from the information theory, to the glacier velocity monitoring by analyzing temporal PolSAR images. In [37], a summary of the dissimilarity measurements for PolSAR image interpretation, is presented; in this paper, the authors discuss and compare the Wishart distance, the Bartlett distance, and the $h - \phi$ family stochastic distances. In [38], a test statistic for equality of two Hermitian positive definite matrices of a complex Wishart distribution, is presented. It can be applied as an edge detection [39]. In [40], a similarity test scheme is proposed for similar pixel detection. In [41] an active contour model using a ratio distance which is defined by using the probability density functions of the regions inside and outside the contours, is proposed. In [42], a distance measure based on the covariance matrix of the Wishart distribution is used to crop estimation.

The geodesic distance (GD) can be used to measure the difference between two parametric distributions. It was presented by Rao [43], [44], and since then it has been studied by several authors [45]–[47]. Berkane *et al.* [48] computed a closed form for the GD between elliptical distributions, but as such forms are not available for every pair of distributions, one has to rely on numerical solutions, e.g., for the GD between two Gamma models [49].

The GD has been used to solve several problems, including multivariate texture retrieval and image classification [50]–[52]. In these articles, the authors compute a closed form for the

J. Naranjo-Torres is with the Coordinación de Física, Instituto Universitario de Tecnología de Maracaibo, Maracaibo 0261, Venezuela (e-mail: josenaranjotorres@gmail.com).

J. Gambini is with the Departamento de Ingeniería Informática, Instituto Tecnológico de Buenos Aires, Buenos Aires C1106ACD, Argentina and also with the Departamento de Ingeniería en Computación, Universidad Nacional de Tres de Febrero, Pcia. de Buenos Aires 77092, Argentina (e-mail: juliana.gambini@gmail.com).

A. C. Frery is with the Laboratório de Computação Científica e Análise Numérica, Universidade Federal de Alagoas, Maceió 57072-970, Brazil (e-mail: acfrery@gmail.com).

GD between multivariate elliptical distributions under certain conditions, including the $\mathcal{G}_{\text{Pol}}^0$ polarimetric distribution [53]. In [54], the authors present a water/land segmentation using the GD, modeling the water and the land with the Gaussian mixed model. Naranjo-Torres *et al.* [55] presented a numerical solution for estimating the GD between samples of \mathcal{G}_I^0 data, under the constraint of unitary mean.

Inspired from these works, we compute closed forms for the GD between \mathcal{G}_I^0 models under certain conditions and we use it as measure of contrast and in edge detection in SAR data. These expressions were not previously available in the literature.

This new approach to measuring the separability between regions of speckled data provides a powerful tool for a number of image processing and understanding problems.

Nascimento *et al.* [29] derived a number of stochastic distances between \mathcal{G}_I^0 laws along the results by Salicru *et al.* [56] and concluded that no analytic expression is, in general, available for them. Among these distances stems the Triangular Distance (TD). Gambini *et al.* [31] concluded that this distance outperforms others from the same class of $(h-\phi)$ distances (Hellinger, Bhattacharyya, and Rényi) in a variety of situations under the \mathcal{G}_I^0 distribution. We compare the GD and the TD, and show that the former presents a number of advantages over the latter. Such comparison is feasible because both GD and TD can be scaled to obey the same limit distribution [46], [56].

The paper unfolds as follows. Section II recalls properties of the \mathcal{G}_I^0 model, including parameter estimation by maximum likelihood. Section III presents the expressions for the GD. Section IV shows the TD and hypothesis tests for both distances. In Section V, we explain the methodology used for edge detection and to assess performance. Section VI shows their application to the discrimination of simulated and actual data. Finally, in Section VII we present conclusions.

II. SPECKLED DATA AND THE \mathcal{G}_I^0 MODEL

Under the multiplicative model, the return in monopolarized SAR images can be described as the product of two independent random variables, one corresponding to the backscatter X and other to the speckle noise Y . In this manner, $Z = XY$ models the return Z in each pixel. For intensity detection, the speckle noise Y is modeled as a Gamma distributed random variable with unitary mean whose shape parameter is the number of looks L . A good choice for the distribution for the backscatter X is the reciprocal of Gamma law that gives rise to the \mathcal{G}^0 distribution for the return Z [21]. This model is an attractive choice for SAR data modeling [57] due to its expresiveness and mathematical tractability.

The probability density function which characterizes the $\mathcal{G}_I^0(\alpha, \gamma, L)$ distribution is

$$f_{\mathcal{G}_I^0}(z) = \frac{L^L \Gamma(L - \alpha)}{\gamma^\alpha \Gamma(-\alpha) \Gamma(L)} \cdot \frac{z^{L-1}}{(\gamma + zL)^{L-\alpha}} \quad (1)$$

where $-\alpha, \gamma, z > 0$ and $L \geq 1$. The r -order moments are

$$E(Z^r) = \left(\frac{\gamma}{L}\right)^r \frac{\Gamma(-\alpha - r)}{\Gamma(-\alpha)} \cdot \frac{\Gamma(L + r)}{\Gamma(L)} \quad (2)$$

provided $\alpha < -r$, and infinite otherwise.

The $\alpha \in \mathbb{R}_-$ parameter describes texture, which is related to the roughness of the target. Values close to zero (typically above -3) suggest extreme textured targets, as urban zones. As the value of α decreases, it indicates regions with moderate texture (usually $\alpha \in [-6, -3]$), as forest zones. Textureless targets, e.g., pasture, usually produce $\alpha \in (-\infty, -6)$.

Let W be a $\mathcal{G}_I^0(\alpha, \gamma, L)$ distributed random variable, then

$$\frac{1}{\gamma} W \sim \mathcal{G}_I^0(\alpha, 1, L) \quad (3)$$

therefore $\gamma \in \mathbb{R}_+$ is a scale parameter.

Given the sample $\mathbf{z} = (z_1, \dots, z_n)$ of independent identically distributed random variables with common distribution $\mathcal{G}_I^0(\alpha, \gamma, L)$ with $(\alpha, \gamma) \in \Theta = \mathbb{R}_- \times \mathbb{R}_+$, a maximum likelihood estimator of (α, γ) satisfies

$$(\hat{\alpha}, \hat{\gamma}) = \arg \max_{(\alpha, \gamma) \in \Theta} \mathcal{L}(\alpha, \gamma, L, \mathbf{z}),$$

where \mathcal{L} is the likelihood function. This leads to $(\hat{\alpha}, \hat{\gamma})$ satisfying

$$\begin{aligned} n[\Psi^0(-\hat{\alpha}) - \Psi^0(L - \hat{\alpha}) - \log \hat{\gamma}] + \sum_{i=1}^n \ln(\hat{\gamma} + Lz_i) &= 0, \\ \frac{n\hat{\alpha}}{\hat{\gamma}} + (L - \hat{\alpha}) \sum_{i=1}^n (\hat{\gamma} + Lz_i)^{-1} &= 0, \end{aligned}$$

where $\Psi^0(t) = d \ln \Gamma(t) / dt$ is the digamma function. In many cases no explicit solution for this system is available and numerical methods are required. We used the Broyden–Fletcher–Goldfarb–Shanno (BFGS) iterative optimization method, which is recommended for solving unconstrained nonlinear optimization problems [58].

III. GEODESIC DISTANCE BETWEEN \mathcal{G}_I^0 MODELS

In this section, we present closed forms for the GD between \mathcal{G}_I^0 distributions.

Let $\theta = (\theta_1, \dots, \theta_r)$, $r \geq 1$ be a parameter in $\Theta \subset \mathbb{R}^r$ and $\{f(z | \theta), \theta \in \Theta\}$ a family of probability density functions of a continuous random variable Z . Under mild regularity conditions, the (i, j) coordinate of the Fisher information matrix [59] is given by

$$g_{ij}(\theta) = -E\left(\frac{\partial^2}{\partial \theta_i \partial \theta_j} \ln f(z | \theta)\right) \quad (4)$$

and the positive definite quadratic differential form

$$ds^2 = \sum_{i,j=1}^d g_{ij}(\theta) d\theta_i d\theta_j \quad (5)$$

can be used as a measure of distance between two distributions whose parameters values are contiguous points of the parameter space.

Consider two parameters $\theta^1, \theta^2 \in \Theta$, and let t be the parameter of a curve $\theta(t) \in \Theta$ which joins θ^1 and θ^2 . Suppose t_1 and t_2 are the values for which $\theta^\ell = \theta(t_\ell)$, $\ell = 1, 2$, then, the GD between two probability distributions can be computed by integrating ds^2 along the geodesics (locally shortest paths) between the corresponding points θ^1 and θ^2 and the GD $s(\theta^1, \theta^2)$

(see [48], [52], [60]) is given by

$$s(\theta^1, \theta^2) = \left| \int_{t_1}^{t_2} \sqrt{\sum_{i,j=1}^r g_{ij}(\theta) \frac{d\theta_i}{dt} \frac{d\theta_j}{dt}} dt \right|. \quad (6)$$

The Fisher information matrix for the $\mathcal{G}_I^0(\alpha, \gamma, L)$ distribution, $g(\alpha, \gamma)$ can be computed from (1) and (4)

$$\begin{pmatrix} \Psi^1(-\alpha) - \Psi^1(L - \alpha) & \frac{L}{L\gamma - \alpha\gamma} \\ \frac{L}{L\gamma - \alpha\gamma} & -\frac{\frac{L\gamma - \alpha\gamma}{L\alpha}}{(L - \alpha + 1)\gamma^2} \end{pmatrix} \quad (7)$$

where Ψ^1 is the trigamma function. The quadratic differential form is obtained from (5) making $r = 2$, $\theta_1 = \alpha$, and $\theta_2 = \gamma$

$$ds^2 = g_{11}(\alpha, \gamma)d\alpha^2 + (g_{12}(\alpha, \gamma) + g_{21}(\alpha, \gamma))d\alpha d\gamma + g_{22}(\alpha, \gamma)d\gamma^2 \quad (8)$$

where $g_{ij}(\alpha, \gamma)$, $i, j \in \{1, 2\}$ are the elements of (7).

In the following, we consider two special cases. We derive the expressions for the GD between \mathcal{G}_I^0 models such that they may differ only on the texture and the scale is known [GD between $\mathcal{G}_I^0(\alpha_1, \gamma^0)$ and $\mathcal{G}_I^0(\alpha_2, \gamma^0)$, γ^0 known], and the only difference between them may be the scale, and the texture is known [GD between $\mathcal{G}_I^0(\alpha^0, \gamma_1)$ and $\mathcal{G}_I^0(\alpha^0, \gamma_2)$, α^0 known].

In the following we derive one-sided test statistics, that can be turned into two-sided test statistics by symmetrization.

A. Geodesic distance for known scale parameter

When γ^0 is known (8) becomes $ds^2 = g_{11}(\alpha, \gamma)d\alpha^2$, thus

$$s(\alpha_1, \alpha_2) = \left| \int_{\alpha_1}^{\alpha_2} \sqrt{\Psi^1(-\alpha) - \Psi^1(L - \alpha)} d\alpha \right| \quad (9)$$

and, using the following property of the trigamma function

$$\Psi^1(-\alpha) - \Psi^1(L - \alpha) = \sum_{n=1}^L (-\alpha + n - 1)^{-2}$$

we obtain

$$s(\alpha_1, \alpha_2) = \left| \int_{\alpha_1}^{\alpha_2} \sqrt{\sum_{n=1}^L (-\alpha + n - 1)^{-2}} d\alpha \right|. \quad (10)$$

This equation can be solved explicitly for $L = \{1, 2\}$.

For $L = 1$, the GD is given by

$$s(\alpha_1, \alpha_2) \Big|_{L=1} = \left| \int_{\alpha_1}^{\alpha_2} \sqrt{\frac{1}{\alpha^2}} d\alpha \right| = \left| \ln \frac{\alpha_2}{\alpha_1} \right|. \quad (11)$$

For $L = 2$, the GD is given by

$$s(\alpha_1, \alpha_2) \Big|_{L=2} = \left| \int_{\alpha_1}^{\alpha_2} \sqrt{\frac{1}{\alpha^2} + \frac{1}{(\alpha - 1)^2}} d\alpha \right| = \left| \ln \frac{\alpha_1^2(\alpha_2 - 1)^2(\alpha_2 R_2 - 1)((\alpha_1 - 1)R_1 + 1)}{\alpha_2^2(\alpha_1 - 1)^2(\alpha_1 R_1 - 1)((\alpha_2 - 1)R_2 + 1)} + \sqrt{2} \ln \frac{1 + \alpha_2(R_2 - 2) - \alpha_2^2 R_2}{1 + \alpha_1(R_1 - 2) - \alpha_1^2 R_1} \right| \quad (12)$$

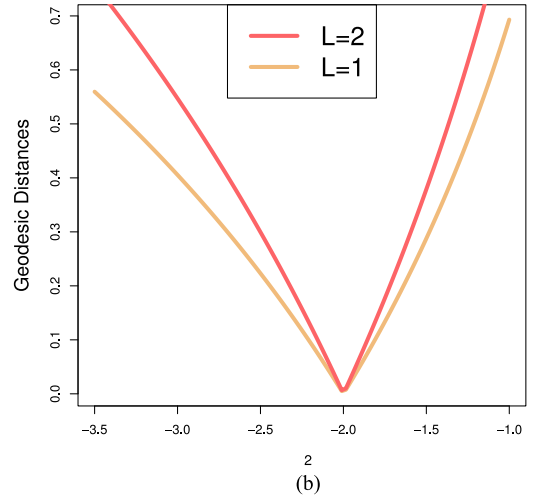
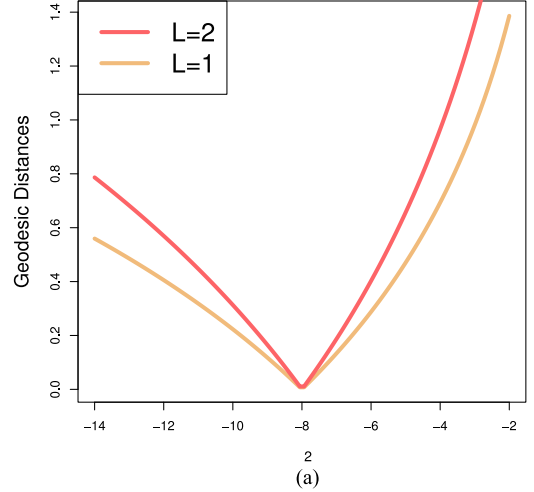


Fig. 1. Geodesic distances between $\mathcal{G}_I^0(\alpha, 1, L)$ distributions for different values of α and L . (a) Geodesic distances, $\alpha_1 = -8$, $\alpha_2 \in [-14, -2]$, and $L = \{1, 2\}$. (b) Geodesic distances, $\alpha_1 = -2$, $\alpha_2 \in [-3.5, -1]$, and $L = \{1, 2\}$.

where

$$R_i = \sqrt{\frac{4\alpha_i^2 - 4\alpha_i + 2}{(\alpha_i - 1)^2 \alpha_i^2}}.$$

Fig. 1(a) shows the GD between $\mathcal{G}_I^0(\alpha, 1, L)$ distributions, $L = \{1, 2\}$, $\alpha_1 = -8$, $\alpha_2 \in [-14, -2]$. Fig. 1(b) shows the GDs between $\mathcal{G}_I^0(\alpha, 1, L)$ distributions, $L = \{1, 2\}$, $\alpha_1 = -2$, $\alpha_2 \in [-3.5, -1]$. Notice their quasi-linear behavior, which is quite different from the quadratic-looking shapes exhibited by the stochastic distances presented in [29].

Larger values of L require numerical integration methods for solving (10). Adaptive integration methods are recommended; cf., the Appendix.

Fig. 2(a) shows the GD between $\mathcal{G}_I^0(\alpha, 1, L)$ distributions, for $L = \{3, 6, 8\}$, $\alpha_1 = -8$, $\alpha_2 \in [-14, -2]$. Fig. 2(b) shows the GDs between $\mathcal{G}_I^0(\alpha, 1, L)$ distributions, $L = \{3, 6, 8\}$, $\alpha_1 = -2$, $\alpha_2 \in [-3.5, -1]$.

In all situations, it is possible to observe that, the smaller the difference between α_1 and α_2 is, the smaller the value of $s(\alpha_1, \alpha_2)$ is. Additionally, it is observed that as the number of

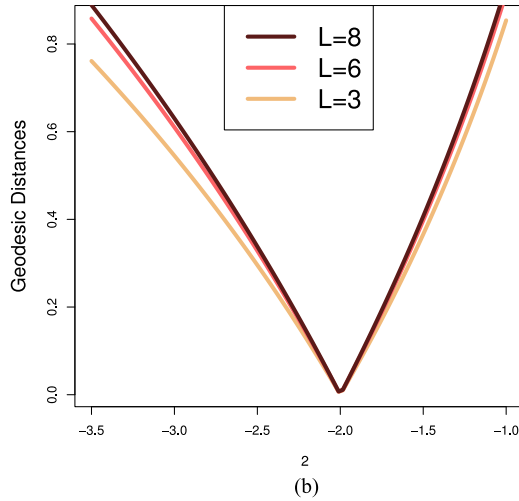
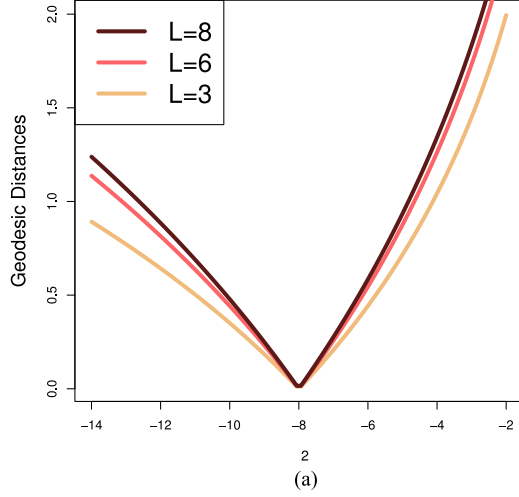


Fig. 2. Geodesic Distance computed numerically using the adaptive integration method for the $\mathcal{G}_I^0(\alpha, 1, L)$ distribution. (a) Geodesic distances, $\alpha_1 = -8, \alpha_2 \in [-14, -2]$ and $L = \{3, 6, 8\}$. (b) Geodesic distances, $\alpha_1 = -2, \alpha_2 \in [-3.5, -1]$ and $L = \{3, 6, 8\}$.

looks increases, the GD $s(\alpha_1, \alpha_2)$ increases, for the same values of α_1 and α_2 . The curve is steeper for larger values of α . This is because for small L , the texture parameter α has stronger influence on the model, causing higher variability than for those situations in which the signal-to-noise ratio is more favorable.

B. Geodesic distance for known texture

In this section, we compute the GD between $\mathcal{G}_I^0(\alpha, \gamma, L)$ models with $\alpha = \alpha^0$ known. In this case (8) becomes $ds^2 = g_{22}(\alpha, \gamma)d\gamma^2$, then the GD is

$$\begin{aligned} s(\gamma_1, \gamma_2) &= \left| \int_{\gamma_1}^{\gamma_2} \sqrt{\frac{-\alpha L}{(-\alpha + L + 1)\gamma^2}} d\gamma \right| \\ &= \left| \sqrt{\frac{-\alpha L}{-\alpha + L + 1}} \ln \frac{\gamma_1}{\gamma_2} \right|. \end{aligned} \quad (13)$$

Notice that, differently from (10), this is a closed expression for every L .

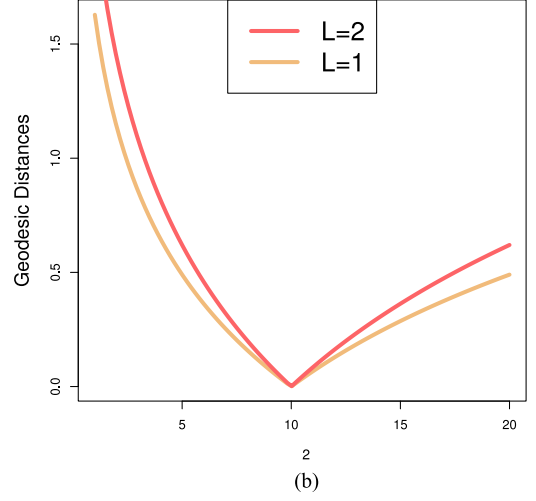
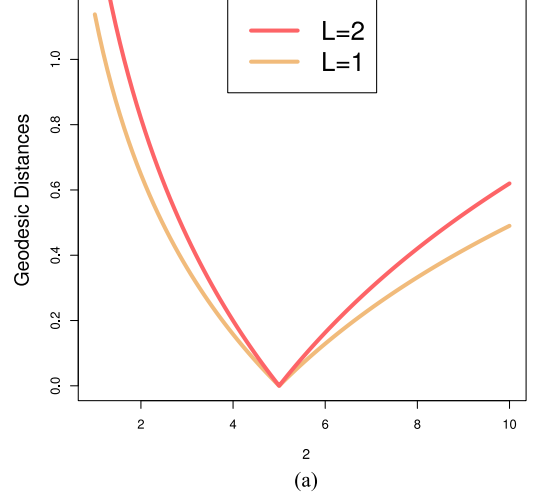


Fig. 3. Geodesic distance between $\mathcal{G}_I^0(\alpha^0, \gamma, L)$ models. (a) Geodesic Distance, $\gamma_1 = 5, \gamma_2 \in [1, 10], \alpha = -2$, and $L = \{1, 2\}$. (b) Geodesic distance, $\gamma_1 = 10, \gamma_2 \in [1, 20], \alpha = -2$, and $L = \{1, 2\}$.

Fig. 3(a) shows the GDs between $\mathcal{G}_I^0(\alpha, \gamma, L)$ models with $L = \{1, 2\}, \alpha = -2, \gamma_1 = 5, \gamma_2 \in [1, 10]$. Fig. 3(b) shows the GDs between models with $L = \{1, 2\}, \alpha = -2, \gamma_1 = 10, \gamma_2 \in [1, 20]$.

IV. TRIANGULAR DISTANCE AND HYPOTHESIS TESTING

An important family of stochastic distances stems from the results by Salicru *et al.* [56], and among them the triangular distance (TD) has been successfully used for SAR data analysis [31].

Consider the densities f_V and f_W with common support S ; the TD between them is given by

$$d_T(f_V, f_W) = \int_S \frac{(f_V(z) - f_W(z))^2}{f_V(z) + f_W(z)} dz. \quad (14)$$

This distance does not have explicit expression in general, and requires the use of numerical integration when applied to two \mathcal{G}_I^0 laws.

So far, we have discussed two distances between \mathcal{G}_I^0 models: GD and TD. As such, they are not comparable and there is

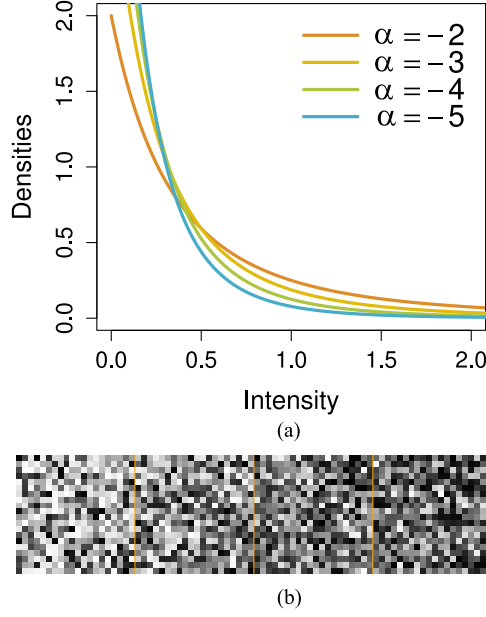


Fig. 4. The $\mathcal{G}_I^0(\alpha, 1, 1)$ model and the data it produces. (a) Densities of the $\mathcal{G}_I^0(\alpha, 1, 1)$ distribution, with different values of α , (b) Data from the $\mathcal{G}_I^0(\alpha, 1, 1)$ distribution, with $\alpha \in \{-2, -3, -4, -5\}$.

no possible semantic interpretation of their values. The forthcoming results transform these distances into test statistics with the same asymptotic distribution and, with this, they become comparable and a tool for hypothesis testing.

Consider two random samples $\mathbf{x} = (x_1, \dots, x_m)$ and $\mathbf{y} = (y_1, \dots, y_n)$ from the $\mathcal{G}_I^0(\alpha_1, \gamma, L)$ and $\mathcal{G}_I^0(\alpha_2, \gamma, L)$ laws, respectively, with γ and L known, and the maximum likelihood estimators $\hat{\alpha}_1$ and $\hat{\alpha}_2$ based on them. Compute the statistics $S_{GD}(\hat{\alpha}_1, \hat{\alpha}_2)$ and $S_{TD}(\hat{\alpha}_1, \hat{\alpha}_2)$ given by

$$S_{GD}(\hat{\alpha}_1, \hat{\alpha}_2) = \frac{mn}{m+n} s^2(\hat{\alpha}_1, \hat{\alpha}_2) \quad (15)$$

$$S_{TD}(\hat{\alpha}_1, \hat{\alpha}_2) = \frac{2mn}{m+n} d_T(\hat{\alpha}_1, \hat{\alpha}_2). \quad (16)$$

Under mild regularity conditions (see [46], [56]), if the null hypothesis $H_0 : \alpha_1 = \alpha_2$ holds these two test statistics obey a χ_1^2 distribution when $m, n \rightarrow \infty$ provided $m(m+n)^{-1} \rightarrow \lambda \in (0, 1)$.

It can be observed that the null hypothesis is equivalent to testing the hypotheses $s(\hat{\alpha}_1, \hat{\alpha}_2) = 0$ and $d_T(\hat{\alpha}_1, \hat{\alpha}_2) = 0$.

Although these results were stated for the case of known scale and number of looks, they are easily extended for other situations.

V. EDGE DETECTION

Discriminating targets by their roughness is a tough task when this is the only difference between them, as presented in Fig. 4. Fig. 4(a) shows the curves of the probability density of the \mathcal{G}_I^0 distribution for different values of α and the same scale and looks, and Fig. 4(b) shows data generated with these models. It can be seen that both the densities and the data are hard to differentiate and, with this, the regions are difficult to distinguish.

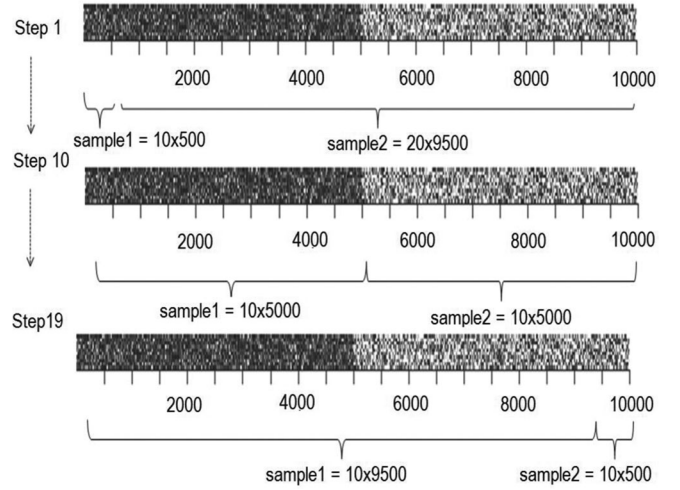


Fig. 5. Simulated image and diagram illustrating the procedure to find the edge point.

We performed a Monte Carlo experiment to assess the discriminatory power between SAR regions through the GD and TD under the \mathcal{G}_I^0 distribution.

We generated $m \times n$ pixels data strips divided in halves: one filled with samples from a $\mathcal{G}_I^0(\alpha_1, \gamma_1, L)$ law, and the other with observations from a $\mathcal{G}_I^0(\alpha_2, \gamma_2, L)$ distribution.

When a good edge detection algorithm is applied to this simulated image, it should give as result the position of the midpoint, which is the transition point.

The number of elements of the sample used to estimate the parameters in the first step, NoE is chosen, so $k_{top} = \lfloor \frac{n}{NoE} \rfloor - 1$ estimation procedures $k = 1, \dots, k_{top}$ are performed over each strip. In each k two samples are produced, $S_1(k)$ and $S_2(k)$, of sizes $m \times NoE * k$ and $m \times (n - NoE * k)$ pixels, respectively. Fig. 5 illustrates this idea, where $m = 10$, $n = 10000$, $NoE = 500$, and $k_{top} = 19$.

Each of these two samples is used to estimate (α, γ) by maximum likelihood, obtaining $(\hat{\alpha}_1(k), \hat{\alpha}_2(k))$ and $(\hat{\gamma}_1(k), \hat{\gamma}_2(k))$. The data in each sample $S_i(k)$ are divided by $\hat{\gamma}_i$, $i = 1, 2$, producing the scaled samples $S_1^*(k)$ and $S_2^*(k)$. According to (3), the data in $S_i^*(k)$ can be approximately described by $\mathcal{G}_I^0(\alpha_i(k), 1, L)$ distributions and, in doing so, the data on both sides have the same mean brightness. New texture estimates are computed with these scaled data, namely $(\hat{\alpha}_1^*(k), \hat{\alpha}_2^*(k))$, and then the distances can be computed between the data in each sample using (10) and (14). These distances are then transformed into test statistics with (15) and (16); this transformation takes into account the different sample sizes used at every step. Notice that, as this application uses test statistics with the same asymptotic distribution, the features and results are comparable.

We then build polygonal curves using the values of S_{GD} and S_{TD} , as control points. Finally, we find the positions at which these curves have the largest value. The method is sketched in Algorithm 1, where m and n are the number of rows and columns of the input image and the variable NoE is the number of sample elements in the first step of the algorithm.

Algorithm 1: Edge Detection through the Geodesic Distance.

- 1: input: m, n, NoE .
- 2: Produce a strip of $m \times n$ pixels divided in halves with data from $\mathcal{G}_I^0(\alpha_1, \gamma_1, L)$ and $\mathcal{G}_I^0(\alpha_2, \gamma_2, L)$.
- 3: $k_{top} = \lfloor \frac{n}{NoE} \rfloor - 1$
- 4: **for** $k = 1, 2, \dots, k_{top}$ **do**
- 5: Produce samples $S_1(k)$ and $S_2(k)$ of sizes $m \times NoE * k$ and $m \times (n - NoE * k)$ pixels from the strip.
- 6: Estimate (α, γ) by maximum likelihood in each sample, obtaining $(\hat{\alpha}_1(k), \hat{\alpha}_2(k))$ and $(\hat{\gamma}_1(k), \hat{\gamma}_2(k))$.
- 7: Divide the values in $S_i(k)$ by $\hat{\gamma}_i$, obtaining $S_i^*(k)$.
- 8: Calculate $(\hat{\alpha}_1^*(k), \hat{\alpha}_2^*(k))$ with the scaled data.
- 9: Compute $s(\hat{\alpha}_1^*(k), \hat{\alpha}_2^*(k))$ and $d_T(\hat{\alpha}_1^*(k), \hat{\alpha}_2^*(k))$ using (10) or its particular cases and Eq. (14), respectively.
- 10: **end for**
- 11: Consider the array of distances between the pairs of samples: $s = \{s(\hat{\alpha}_1^*(k), \hat{\alpha}_2^*(k)), 1 \leq k \leq k_{top}\}$ and $d_T = \{d_T(\hat{\alpha}_1^*(k), \hat{\alpha}_2^*(k)), 1 \leq k \leq k_{top}\}$.
- 12: Transform distances into tests statistics with (15) and (16) obtaining the arrays S_{GD} and S_{TD} from s and d_T , respectively.
- 13: Find the transition points where the test statistics are maximized:

$$\hat{p}_s = \arg \max_k S_{GD},$$

$$\hat{p}_T = \arg \max_k S_{TD}.$$

Notice that this procedure provides a coarse estimation of the underlying distance between the patches. In practical applications, as those discussed by [25], [30], [32], a finer search strategy must be employed.

VI. RESULTS

In this section, we present the results of applying the features and methods described in previous sections. We use simulated and actual data, and we compare the performance of the GD with respect to the TD.

A. Results With Simulated Data

The procedure sketched in Algorithm 1 was repeated 1000 times over strips obtained with different texture and looks parameters, independently. Fig. 6 shows the mean polygonal curves obtained in each situation by computing S_{GD} and S_{TD} .

It can be seen that the transition, which is indicated with a vertical dotted line, can be estimated from these polygonal curves as it is consistently the largest value.

The evidence provided by the S_{GD} is more conclusive that coming from S_{TD} , as can be seen comparing the solid and dotted lines of same color. In particular, the TD provides little or no evidence to find the edge between $\alpha_1 = -2$ and $\alpha_2 = -3$ and $L = 2$.

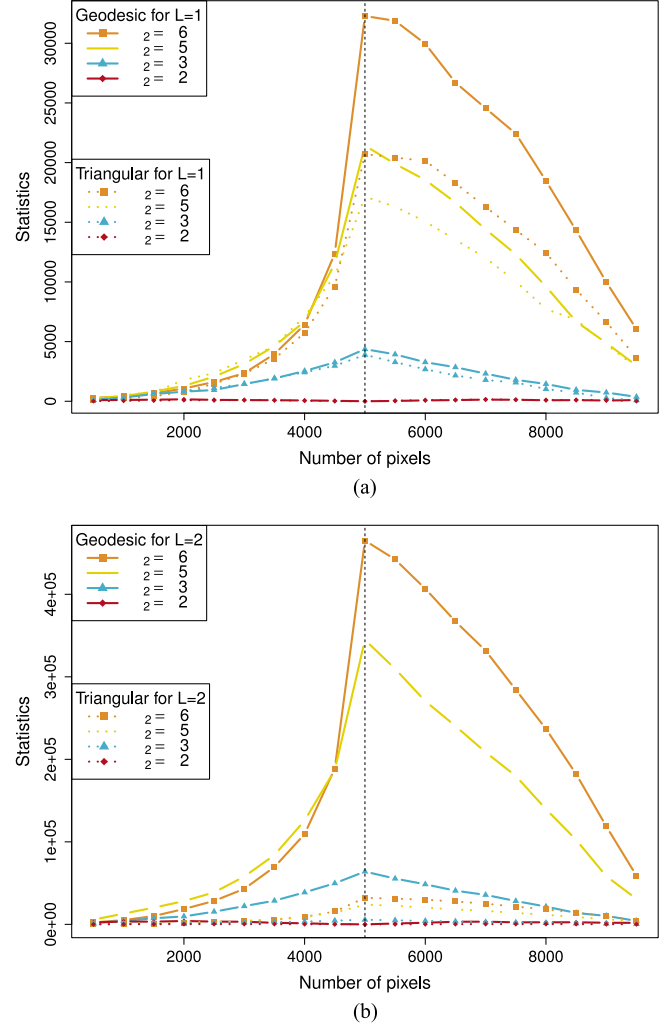


Fig. 6. Test statistics based on the Geodesic and Triangular distances between potentially mixed samples from $\mathcal{G}_I^0(-2, 1, L)$ and $\mathcal{G}_I^0(\alpha_2, 1, L)$ laws, with $\alpha_2 = \{-2, -3, -5, -6\}$. (a) Mean polygonal curves for $L = 1$. (b) Mean polygonal curves for $L = 2$.

In addition, the larger the difference between α_1 and α_2 is, the larger are the values of the maxima.

The procedure is, thus, able to identify the position of the transition point between areas with different texture and same mean brightness, a difficult task in edge detection.

We also studied the case where there is no edge, i.e., $\alpha_1 = \alpha_2 = -2$. The polygonal curves are shown in dark red, and they are, for both distances and looks, the smallest. These curves do not exhibit either global or local maxima that may lead to erroneous identification of edges. The proposal is, thus, overall not prone to producing false alarms.

B. Empirical p-Values

Although the asymptotic distribution of (15) and (16) is known, it is also valuable to know about their finite size sample behavior.

Two samples of the same distribution ($\alpha_1 = \alpha_2 = -1.5$, $\gamma = 1$ and $L = 1$) and same size were generated, and the number of cases for which the test statistics produced values larger

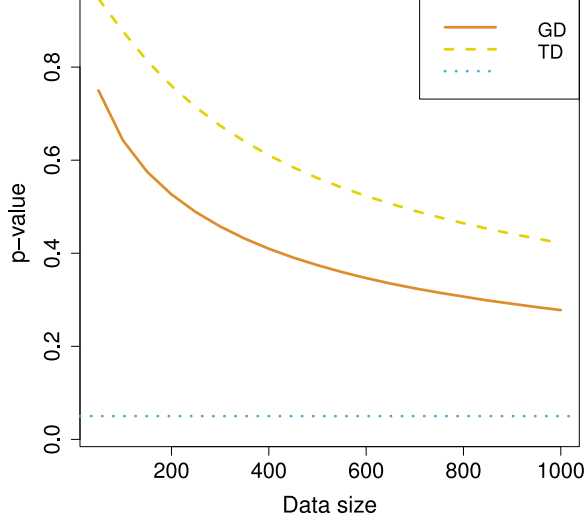


Fig. 7. Empirical p -values for different sample sizes.

than the critical one at 5%, namely, 3.841459. This was repeated 5000 times, and the results are shown in Fig. 7.

Both tests tend to reject less than expected, since the empirical p -values are larger than the asymptotic one. The test based on the GD, S_{GD} converges faster to $\eta = 0.05$ than the one that relies on the TD. It is also consistently closer to the asymptotic value.

C. Results With Actual Data

In the following, we show the results of applying the proposed technique to an E-SAR image [61] from the surroundings of Munich, Germany. We employed L band, HH polarization in single-look complex format to produce intensity data. The original resolution is $2.2 \text{ m} \times 3.0 \text{ m}$ (range \times azimuth). The intensity of each pixel is henceforth referred to as “full resolution” data; the subsampled average of four contiguous pixels is “reduced resolution.” Theoretically, the former has one look while the latter has four looks.

Fig. 8(a) shows the SAR image, and presents the area where the edge detection was performed. Fig. 8(b) is the corresponding optical image from Google Maps. Fig. 8(c) shows the result of applying the edge detector with both GD and TD to equally-spaced horizontal strips of side 3. It is remarkable that both led to the same edge points, differing only in the time it took to calculate them, except when the integral of the TD does not converge and therefore it returns no result. The computation time of TD is 70 times larger the computation time of GD, and it fails to converge with small samples. Fig. 8(d) shows the edge detection using only GD, to the reduced resolution image. It can be seen that two points are shifted from the right place, but the result is acceptable.

In order to show the advantage of our method, the ROA edge detector proposed by Touzi *et al.* [62] was applied to the same data of Figs. 8(c) and (d).

The results are shown in Figs. 9(a) and (b). The parameters used are: 1) increasing window size: 3×3 , 5×5 , and 7×7 , 2) lower and higher thresholds: 0.14 and 0.22,

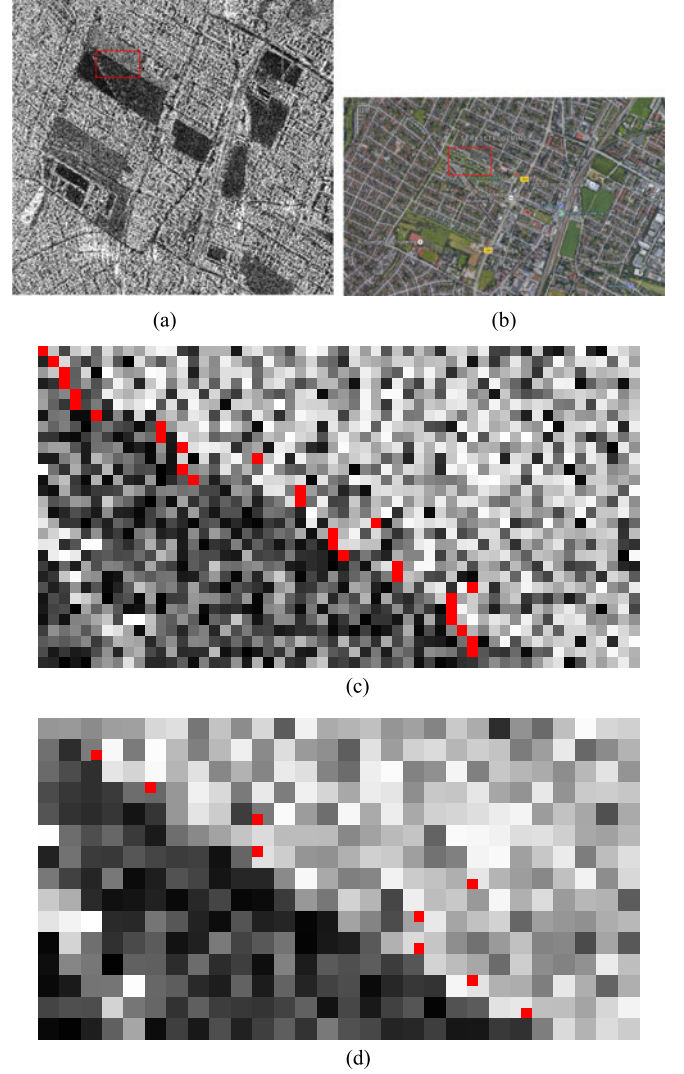
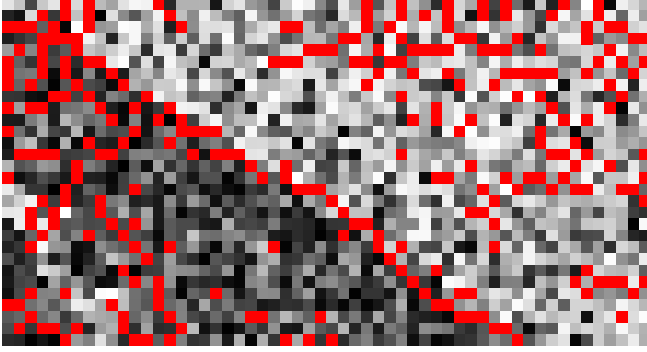


Fig. 8. Results of applying the edge detectors to actual data. (a) SAR image and the region used in Figs. 8(c) and 9(a). (b) The corresponding optical image from Google Maps. (c) Edge points found over each line of the image with the GD and TD. (d) Edge points found in the image with lower resolution, with the GD.

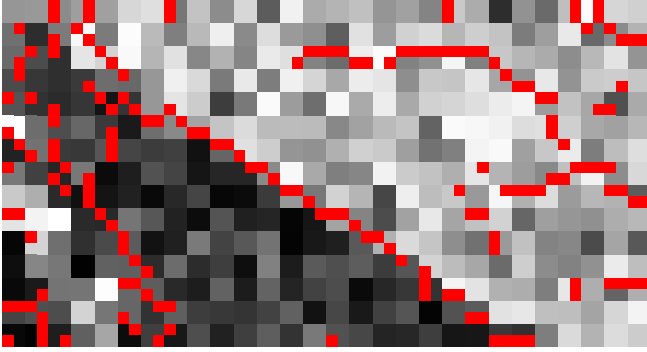
respectively. When compared to the edge points obtained using distances, ROA produces noisier results with higher false alarm results. ROA improves when applied to the reduced resolution data set, in agreement with the fact that this method is especially designed to segment smooth targets.

In the following, we discuss the effect of reducing the resolution on the distances using two actual images.

Fig. 10 presents the samples used to estimate the parameters, and to then measure GD and TD between them. We identified five samples: A1 and A5 correspond to pasture regions, A2 and A4 areas are forest regions, and A3 corresponds to an urban region. We estimated the texture parameter α of the \mathcal{G}_l^0 distribution in both full and reduced resolution; denote the estimates $\hat{\alpha}$ and $\hat{\alpha}_{RR}$ (reduced resolution), respectively. These estimates are shown in Table I, and help in the identification of the types of land cover because they are related to the area roughness.



(a)



(b)

Fig. 9. Results of applying the Touzi edge detectors to actual data. (a) Result of the Touzi edge detector, full resolution data. (b) Result of the Touzi edge detector, reduced resolution data.



Fig. 10. Regions from E-SAR data used to extract the proposed features.

The table also shows the size of each sample in full resolution (the reduced resolution samples are one fourth of the original size).

These estimates are consistent with the land cover types visually identified. The estimates reduce with the resolution in most cases; this is in agreement with the fact that the reduced

TABLE I
ESTIMATES OF α IN AREAS FROM THE IMAGE IN FIG. 10

Sample	Sample Size	$\hat{\alpha}$	$\hat{\alpha}_{RR}$
A1	1360	-6.09	-11.53
A2	1225	-9.72	-20.00
A3	2088	-1.01	-1.00
A4	1824	-2.75	-4.27
A5	1152	-11.51	-20.00

TABLE II
DISTANCES BETWEEN MODELS FOR ACTUAL DATA

		Sample	A2	A3	A4	A5
Full Resolution	GD	A1	0.467	1.807	0.794	0.636
		A2	0	2.274	1.261	0.169
		A3		0	1.013	2.443
		A4			0	1.430
	TD	A1	0.097	0.840	0.248	0.170
		A2	0	1.097	0.515	0.014
		A3		0	0.367	1.182
		A4			0	0.617
Reduced Resolution	GD	A1	2.277	12.503	4.004	2.277
		A2	0	14.781	6.282	0
		A3		0	8.498	14.781
		A4			0	6.282
	TD	A1	0.238	1.524	0.584	0.238
		A2	0	1.743	1.061	0
		A3		0	0.854	1.743
		A4			0	1.061

resolution data were obtained by smoothing the observations. This change reflects on changes in the distances.

Table II presents the distances between regions in both full and reduced resolution.

Table II shows that the largest and smallest distances correspond to areas with very different texture and to two smooth areas, respectively. This indicates that region discrimination by means of both GD and TD is possible, as they behave as expected. The distances change when the resolution changes, but the largest and smallest values of both GD and TD are still between A3 and A5, and A2 and A5, respectively, which indicates that the capability of texture discrimination is not affected by changes in the image resolution.

Table II also reveals that the GD is more sensitive to differences in the texture parameter values, allowing a finer discrimination between pasture and forest areas. The TD correctly discriminates regions having very different texture, such as A3 (extreme textured area) and A5 (textureless area) but in the case of A1 and A2 which correspond to a textureless area and a moderate textured area, respectively, TD loses the ability to separate: its value is almost zero. This implicates an advantage of GD over TD.

Fig. 11 illustrates the distances between A1 and the other regions in both full and reduced resolution. GD and TD are represented with orange and green colors, respectively. The line thickness is proportional to the distances between region models.

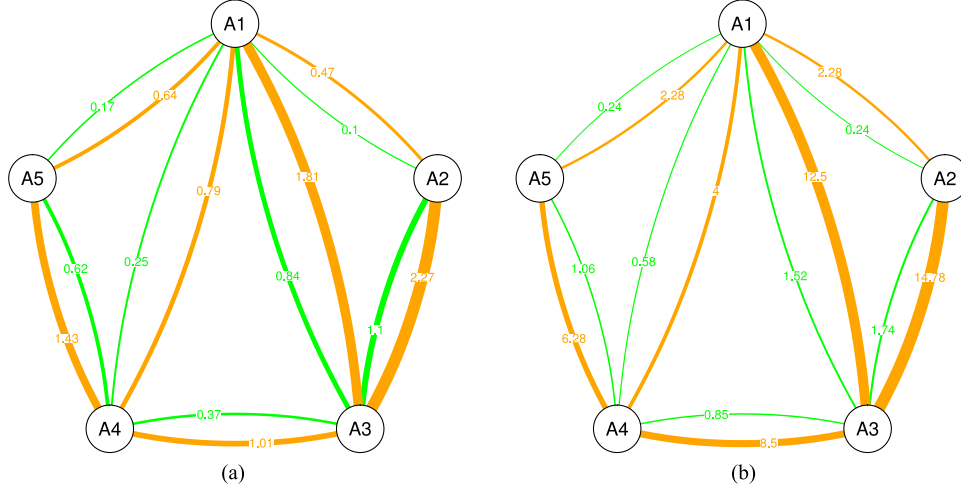


Fig. 11. Illustration distances between samples of true data in full and reduced resolution: GD in orange, and TD in green. (a) Distances between models for full resolution data. (b) Distances between models for reduced resolution data.

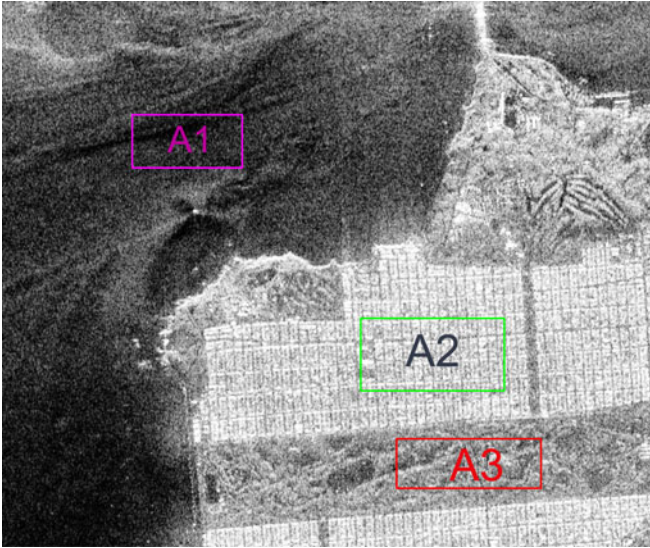


Fig. 12. AIRSAR data over San Francisco, USA.

TABLE III
ESTIMATES OF α IN SAMPLES FROM FIG. 12

Sample	Sample Size	$\hat{\alpha}$	$\hat{\alpha}_{RR}$
A1	12282	-11.307	-11.488
A2	8266	-2.016	-2.558
A3	7878	-5.746	-6.485

Fig. 12 shows an AIRSAR image over San Francisco, USA, HH polarization in intensity, with the equivalent number of looks $\hat{L} = 2$. We identified three samples: A1 corresponding to water, A2 an urban region, and A3 a forest area. The same procedure was performed as before for obtaining an image with reduced resolution. Table III shows the estimates of the α parameter for each region and the sample size, for both resolutions. It can be seen that the estimates agree with the visual interpretation of the classes.

TABLE IV
DISTANCES BETWEEN MODELS FOR ACTUAL DATA

		Sample	A2	A3
Full Res.	GD	A1	6.86	2.74
		A2	0	4.12
	TD	A1	1.14	0.32
		A2	0	0.58
Red. Res.	GD	A1	8.13	3.22
		A2	0	4.91
	TD	A1	1.29	0.38
		A2	0	0.69

Table IV presents the GD and the TD between regions. This example highlights the difficulty TD has to distinguish regions with a similar roughness. It can be seen that the TD between A1 and A3 and between A2 and A3 are almost the same in both resolutions.

These experiments show that the methodology is not affected if the image has reduced resolution. Furthermore, as the integral of the TD is calculated numerically, the computational cost is higher and it may even not converge, which is another advantage of the GD over the TD.

VII. CONCLUSION

This paper is dedicated to deriving the geodesic distance (GD) between \mathcal{G}_I^0 models, a result that fills a gap in the literature of contrast measures for this distribution. This distance can be used as a feature for, among other applications, edge detection in speckled data.

We derived a closed formula for the geodesic distance for $L = \{1, 2\}$, and we provide the general expression that can be used in other cases relying to numerical integration. The unknown parameters were estimated using maximum likelihood to grant interesting asymptotic properties for the GD. We compared the geodesic and triangular (TD) distances, with favorable results for the first over the second.

It is possible to observe that, as the lower difference between α_1 and α_2 is, the lower value of $s(\alpha_1, \alpha_2)$ is, which indicates that this distance is an appropriate feature to measure the contrast between regions.

The results of applying the GD for edge detection in simulated images are excellent. Computing GD requires about 70 times less computational time than TD.

When dealing with actual data from two sensors and two different scenes, large values of the GD and TD come from areas of the image with different roughness, but TD is consistently smaller than GD, making more difficult the identification of such differences.

The effectiveness of using GD is not affected by the resolution, but going beyond $L = 2$ increases the computational cost for its calculation since numerical methods are required.

The value of γ does not affect the results because it is a scale parameter of the \mathcal{G}_I^0 distribution.

One may transform GD and TD into test statistics with the same asymptotic distribution and, with this, they become comparable and tools for hypothesis testing. The finite-size behavior of the tests, cf., Fig. 7, suggests the need of corrections in order to make them closer to the asymptotic result, but we observed that GD converges faster than TD to the asymptotic critical value.

As future work, we will experiment with contaminated data to measure the robustness of GD.

APPENDIX

Simulations were performed using the R language and environment for statistical computing version 3.3. [63], in a computer with processor Intel® Core™, i7-4790K CPU 4 GHz, 16GB RAM, System Type 64 bit operating system.

The numerical integration required to evaluate the geodesic distance for $L \neq 1, 2$, and the triangular distance was performed with the `adaptIntegrate` function from the `cubature` package. This is an adaptive multidimensional integration over hypercubes.

The Google Maps link for the image of Fig. 10 is <https://goo.gl/maps/DCm6fBKcRy32>.

ACKNOWLEDGMENT

Codes and data are available upon request from the corresponding author.

REFERENCES

- [1] T. Esch *et al.*, "Identification and characterization of urban structures using VHR SAR data," in *Proc. IEEE Int. Geosci. Remote Sens. Symp.*, 2011, pp. 1413–1416.
- [2] Q. Wu, R. Chen, H. Sun, and Y. Cao, "Urban building density detection using high resolution SAR imagery," in *Proc. Joint Urban Remote Sensing Event*, 2011, pp. 45–48.
- [3] C. D. Storie, J. Storie, and G. S. de Salmuni, "Urban boundary extraction using 2-component polarimetric SAR decomposition," in *Proc. IEEE Int. Geosci. Remote Sens. Symp.*, 2012, pp. 5741–5744.
- [4] F. Dell'Acqua and P. Gamba, "Remote sensing and earthquake damage assessment: Experiences, limits, and perspectives," *Proc. IEEE*, vol. 100, no. 10, pp. 2876–2890, Oct. 2012.
- [5] M. Sato, S. W. Chen, and M. Satake, "Polarimetric SAR analysis of tsunami damage following the march 11, 2011 East Japan earthquake," *Proc. IEEE*, vol. 100, no. 10, pp. 2861–2875, Oct. 2012.
- [6] Y. Yamaguchi, "Disaster monitoring by fully polarimetric SAR data acquired with ALOS-PALSAR," *Proc. IEEE*, vol. 100, no. 10, pp. 2851–2860, Oct. 2012.
- [7] S. W. Chen and M. Sato, "Tsunami damage investigation of built-up areas using multitemporal spaceborne full polarimetric SAR images," *IEEE Trans. Geosci. Remote Sens.*, vol. 51, no. 4, pp. 1985–1997, Apr. 2013.
- [8] W. Sun, L. Shi, J. Yang, and P. Li, "Building collapse assessment in urban areas using texture information from postevent SAR data," *IEEE J. Sel. Topics Appl. Earth Observ. Remote Sens.*, vol. 9, no. 8, pp. 3792–3808, Aug. 2016.
- [9] C. Fu, Y. Chen, L. Tong, M. Jia, L. Tan, and X. Ji, "Road damage information extraction using high-resolution SAR imagery," in *Proc. IEEE Geosci. Remote Sens. Symp.*, 2014, pp. 1836–1838.
- [10] M. Barber, C. López-Martínez, and F. Grings, "Assessment of L-Band SAR polarimetry for soil and crop monitoring," in *Proc. Eur. Conf. Synth. Aperture Radar*, Jun. 2016, pp. 1–4.
- [11] R. T. Melrose, R. T. Kingsford, and A. K. Milne, "Using radar to detect flooding in arid wetlands and rivers," in *Proc. IEEE Int. Geosci. Remote Sens. Symp.*, 2012, pp. 5242–5245.
- [12] D. Velotto, S. Lehner, A. Soloviev, and C. Maingot, "Analysis of oceanic features from dual-polarization high resolution X-band SAR imagery for oil spill detection purposes," in *Proc. IEEE Int. Geosci. Remote Sens. Symp.*, 2012, pp. 2841–2844.
- [13] S. Chen, Y. Li, and X. Wang, "Crop discrimination based on polarimetric correlation coefficients optimization for PolSAR data," *Int. J. Remote Sens.*, vol. 36, no. 16, pp. 4233–4249, 2015.
- [14] S.-E. Park, L. Ferro-Famil, S. Allain, and E. Pottier, "Surface roughness and microwave surface scattering of high-resolution imaging radar," *IEEE Geosci. Remote Sens. Lett.*, vol. 12, no. 4, pp. 756–760, Apr. 2015.
- [15] M. Presa, J. Amores, D. Mata Moya, and J. Brcena Humanes, "Statistical analysis of SAR sea clutter for classification purposes," *Remote Sens.*, vol. 6, no. 10, pp. 9379–9411, 2014.
- [16] A. Farrouki and M. Barkat, "Automatic censoring CFAR detector based on ordered data variability for nonhomogeneous environments," *Inst. Electr. Eng. Proc. Radar, Sonar Navig.*, vol. 152, no. 1, pp. 43–51, Feb. 2005.
- [17] J.-S. Lee and I. Jurkevich, "Segmentation of SAR images," *IEEE Trans. Geosci. Remote Sens.*, vol. 27, no. 6, pp. 674–680, Nov. 1989.
- [18] R. Fjørtoft, Y. Delignon, W. Pieczynski, M. Sigelle, and F. Tupin, "Unsupervised classification of radar images using hidden Markov chains and hidden Markov random fields," *IEEE Trans. Geosci. Remote Sens.*, vol. 41, no. 3, pp. 675–686, Mar. 2003.
- [19] P. X. Vu, N. T. Duc, and V. V. Yem, "Application of statistical models for change detection in SAR imagery," in *Proc. Int. Conf. Commun., Manage. Telecommun.*, 2015, pp. 239–244.
- [20] J. Gambini, M. Mejail, J. Jacobo-Berlles, and A. Frery, "Feature extraction in speckled imagery using dynamic B-spline deformable contours under the \mathcal{G}^0 model," *Int. J. Remote Sens.*, vol. 27, no. 22, pp. 5037–5059, 2006.
- [21] A. C. Frery, H.-J. Müller, C. C. F. Yanasse, and S. J. S. Sant'Anna, "A model for extremely heterogeneous clutter," *IEEE Trans. Geosci. Remote Sens.*, vol. 35, no. 3, pp. 648–659, May 1997.
- [22] Y. Wang, T. L. Ainsworth, and J. S. Lee, "On characterizing high-resolution SAR imagery using kernel-based mixture speckle models," *IEEE Geosci. Remote Sens. Lett.*, vol. 12, no. 5, pp. 968–972, May 2015.
- [23] M. Mejail, J. C. Jacobo-Berlles, A. C. Frery, and O. H. Bustos, "Classification of SAR images using a general and tractable multiplicative model," *Int. J. Remote Sens.*, vol. 24, no. 18, pp. 3565–3582, 2003.
- [24] G. Gao, "Statistical modeling of SAR images: A survey," *Sensors*, vol. 10, no. 1, pp. 775–795, 2010.
- [25] J. Gambini, M. Mejail, J. Jacobo-Berlles, and A. C. Frery, "Accuracy of edge detection methods with local information in speckled imagery," *Stat. Comput.*, vol. 18, no. 1, pp. 15–26, 2008.
- [26] W. B. Silva, C. C. Freitas, S. J. S. Sant'Anna, and A. C. Frery, "Classification of segments in PolSAR imagery by minimum stochastic distances between Wishart distributions," *IEEE J. Sel. Topics Appl. Earth Observ. Remote Sens.*, vol. 6, no. 3, pp. 1263–1273, Jun. 2013.
- [27] L. Gomez, L. Alvarez, L. Mazorra, and A. C. Frery, "Classification of complex Wishart matrices with a diffusion-reaction system guided by stochastic distances," *Philosoph. Trans. Royal Soc. A, Math., Phys. Eng. Sci.*, vol. 373, no. 2056, pp. 20150118–20150132, 2015.
- [28] A. C. Frery, R. J. Cintra, and A. D. C. Nascimento, "Entropy-based statistical analysis of PolSAR data," *IEEE Trans. Geosci. Remote Sens.*, vol. 51, no. 6, pp. 3733–3743, Jun. 2013.
- [29] A. D. C. Nascimento, R. J. Cintra, and A. C. Frery, "Hypothesis testing in speckled data with stochastic distances," *IEEE Trans. Geosci. Remote Sens.*, vol. 48, no. 1, pp. 373–385, Jan. 2010.

- [30] A. D. C. Nascimento, M. M. Horta, A. C. Frery, and R. J. Cintra, "Comparing edge detection methods based on stochastic entropies and distances for PolSAR imagery," *IEEE J. Sel. Topics Appl. Earth Observ. Remote Sens.*, vol. 7, no. 2, pp. 648–663, Feb. 2014.
- [31] J. Gambini, J. Cassetti, M. Lucini, and A. Frery, "Parameter estimation in SAR imagery using stochastic distances and asymmetric kernels," *IEEE J. Sel. Topics Appl. Earth Observ. Remote Sens.*, vol. 8, no. 1, pp. 365–375, Jan. 2015.
- [32] E. Girón, A. C. Frery, and F. Cribari-Neto, "Nonparametric edge detection in speckled imagery," *Math. Comput. Simul.*, vol. 82, pp. 2182–2198, 2012.
- [33] R. H. Nobre, F. A. A. Rodrigues, R. C. P. Marques, J. S. Nobre, J. F. S. R. Neto, and F. N. S. Medeiros, "SAR image segmentation with Renyi's entropy," *IEEE Signal Process. Lett.*, vol. 23, no. 11, pp. 1551–1555, Nov. 2016.
- [34] X. Huang, P. Huang, L. Dong, H. Song, and W. Yang, "Saliency detection based on distance between patches in polarimetric SAR images," in *Proc. IEEE Int. Geosci. Remote Sens. Symp.*, 2014, pp. 4572–4575.
- [35] L. Torres, S. J. S. Sant'Anna, C. C. Freitas, and A. C. Frery, "Speckle reduction in polarimetric SAR imagery with stochastic distances and nonlocal means," *Pattern Recognit.*, vol. 47, pp. 141–157, 2014.
- [36] E. Erten, "Glacier velocity estimation by means of a polarimetric similarity measure," *IEEE Trans. Geosci. Remote Sens.*, vol. 51, no. 6, pp. 3319–3327, Jun. 2013.
- [37] W. Yang, H. Song, G. S. Xia, and C. López-Martínez, "Dissimilarity measurements for processing and analyzing PolSAR data: A survey," in *Proc. IEEE Int. Geosci. Remote Sens. Symp.*, 2015, pp. 1562–1565.
- [38] K. Conradsen, A. A. Nielsen, J. Schou, and H. Skriver, "A test statistic in the complex Wishart distribution and its application to change detection in polarimetric SAR data," *IEEE Trans. Geosci. Remote Sens.*, vol. 41, no. 1, pp. 4–19, Jan. 2003.
- [39] J. Schou, H. Skriver, A. A. Nielsen, and K. Conradsen, "CFAR edge detector for polarimetric SAR images," *IEEE Trans. Geosci. Remote Sens.*, vol. 41, no. 1, pp. 20–32, Jan. 2003.
- [40] S. W. Chen, X. S. Wang, and M. Sato, "PolInSAR complex coherence estimation based on covariance matrix similarity test," *IEEE Trans. Geosci. Remote Sens.*, vol. 50, no. 11, pp. 4699–4710, Nov. 2012.
- [41] S. Tu, Y. Li, and Y. Su, "Ratio- and distribution-metric-based active contours for SAR image segmentation," in *Proc. 5th Int. Conf. Intell. Control Inf. Process.*, 2014, pp. 227–232.
- [42] L. Mascolo, J. M. Lopez-Sanchez, F. Vicente-Guijalba, F. Nunziata, M. Migliaccio, and G. Mazzarella, "A complete procedure for crop phenology estimation with PolSAR data based on the complex wishart classifier," *IEEE Trans. Geosci. Remote Sens.*, vol. 54, no. 11, pp. 6505–6515, Nov. 2016.
- [43] C. R. Rao, "Information and the accuracy attainable in the estimation of statistical parameters," *Bull. Calcutta Math. Soc.*, vol. 37, pp. 81–91, 1945.
- [44] C. R. Rao, "Information and the accuracy attainable in the estimation of statistical parameters," in *Breakthroughs in Statistics* (Springer Series in Statistics), S. Kotz and N. L. Johnson, Eds. New York, NY, USA: Springer, 1992, pp. 235–247.
- [45] G. Verdoolaege and P. Scheunders, "On the geometry of multivariate generalized gaussian models," *J. Math. Imag. Vis.*, vol. 43, no. 3, pp. 180–193, 2012.
- [46] M. L. Menéndez, D. Morales, L. Pardo, and M. Salicrú, "Statistical test based on the geodesic distances," *Appl. Math. Lett.*, vol. 8, no. 1, pp. 65–69, 1995.
- [47] C. Atkinson and A. F. S. Mitchell, "Rao's distance measure," *Sankhyā, Indian J. Statist., Series A*, vol. 43, pp. 345–365, 1981.
- [48] M. Berkane, K. Oden, and P. Bentler, "Geodesic estimation in elliptical distributions," *J. Multivariate Anal.*, vol. 63, pp. 35–46, 1997.
- [49] F. Reverter and J. Oller, "Computing the Rao distance for Gamma distributions," *J. Comput. Appl. Math.*, vol. 157, no. 1, pp. 155–167, 2003.
- [50] L. Bombrun, Y. Berthoumieu, N.-E. Lasmar, and G. Verdoolaege, "Multivariate texture retrieval using the geodesic distance between elliptically distributed random variables," in *Proc. 18th IEEE Int. Conf. Image Process.*, 2011, pp. 3637–3640.
- [51] A. D. El Maliani, M. El Hassouni, Y. Berthoumieu, and D. Aboutajdine, "Color texture classification method based on a statistical multi-model and geodesic distance," *J. Visual Commun. Image Represent.*, vol. 25, no. 7, pp. 1717–1725, 2014.
- [52] L. Bombrun, N.-E. Lasmar, Y. Berthoumieu, and G. Verdoolaege, "Multivariate texture retrieval using the SIRV representation and the geodesic distance," in *Proc. IEEE Int. Conf. Acoust., Speech Signal Process.*, 2011, pp. 865–868.
- [53] C. C. Freitas, A. C. Frery, and A. H. Correia, "The polarimetric G distribution for SAR data analysis," *Environmetrics*, vol. 16, no. 1, pp. 13–31, 2005.
- [54] H. Zhong, Q. Xie, L. Jiao, and S. Wang, "Water/land segmentation for SAR images based on geodesic distance," in *Proc. IEEE Int. Geosci. Remote Sens. Symp.*, 2011, pp. 2661–2664.
- [55] J. Naranjo-Torres, J. Gambini, and A. C. Frery, "Region discrimination in SAR imagery using the geodesic distance between G_{10} distributions," in *Proc. IEEE 5th Asia-Pacific Conf. Synth. Aperture Radar*, 2015, pp. 573–577.
- [56] M. Salicrú, D. Morales, M. L. Menéndez, and L. Pardo, "On the applications of divergence type measures in testing statistical hypotheses," *J. Multivariate Anal.*, vol. 51, no. 2, pp. 372–391, 1994.
- [57] M. Quartulli and M. Datcu, "Stochastic geometrical modelling for built-up area understanding from a single SAR intensity image with meter resolution," *IEEE Trans. Geosci. Remote Sens.*, vol. 42, no. 9, pp. 1996–2003, Sep. 2004.
- [58] C. G. Broyden, "A class of methods for solving nonlinear simultaneous equations," *Math. Comput.*, vol. 19, pp. 577–593, 1965.
- [59] O. Besson and Y. I. Abramovich, "On the Fisher information matrix for multivariate elliptically contoured distributions," *IEEE Signal Process. Lett.*, vol. 20, no. 11, pp. 1130–1133, Nov. 2013.
- [60] G. Marti, S. Andler, F. Nielsen, and P. Donnat, "Optimal transport vs. Fisher-Rao distance between copulas for clustering multivariate time series," in *Proc. IEEE Statist. Signal Process. Workshop*, 2016, pp. 1–5.
- [61] R. Horn, "E-SAR: The experimental airborne L/C-band SAR system of DFVLR," in *Proc. IEEE Int. Geosci. Remote Sens. Symp.*, 1988, vol. 2, pp. 1025–1026.
- [62] R. Touzi, A. Lopes, and P. Bousquet, "A statistical and geometrical edge detector for SAR images," *IEEE Trans. Geosci. Remote Sens.*, vol. 26, no. 11, pp. 764–773, Nov. 1988.
- [63] R Core Team, "R: A Language and Environment for Statistical Computing," Roy. Found. Statist. Comput., Vienna, Austria, 2016. [Online]. Available: <https://www.R-project.org/>



José Naranjo-Torres received the B.Sc. degree in physics and the M.Sc. degree in geophysics both from the Universidad del Zulia, Venezuela, in 1996 and 2004, respectively.

He is an Aggregated Professor at the Instituto Universitario de Tecnología de Maracaibo, Venezuela. He is currently working toward the Ph.D. degree in the Universidad Nacional de General Sarmiento, Pcia. de Buenos Aires, Argentina. His research interests include statistical models for image processing and geophysics.



Juliana Gambini received the B.Sc. degree in mathematics and the Ph.D. degree in computer science both from Universidad de Buenos Aires, Argentina, in 1996 and 2006, respectively.

She is currently working as a Titular Professor at the Instituto Tecnológico de Buenos Aires (ITBA), Buenos Aires, Argentina, member of the Center for Computational Intelligence—ITBA, and a Titular Professor at Universidad Nacional de Tres de Febrero, Pcia. de Buenos Aires, Argentina. Her research interests include SAR image processing, video

processing, and image recognition.



Alejandro C. Frery (S'92–SM'03) received the B.Sc. degree in electronic and electrical engineering from the Universidad de Mendoza, Mendoza, Argentina, in 1985, the M.Sc. degree in applied mathematics (Statistics) from the Instituto de Matemática Pura e Aplicada (IMPA, Rio de Janeiro), in 1990, and the Ph.D. degree in applied computing from the Instituto Nacional de Pesquisas Espaciais (INPE, São José dos Campos, Brazil), in 1993.

He is currently the leader of LaCCAN – *Laboratório de Computação Científica e Análise Numérica*, Universidade Federal de Alagoas, Maceió, Brazil. His research interests include statistical computing and stochastic modeling.